Supplementary Information for "Mechanics of cellular packing of nanorods with finite and non-uniform diameters"

Xin Yi,[*,†] Guijin Zou,[‡] and Huajian Gao[*,‡]

[†]College of Engineering and BIC-ESAT, Peking University, Beijing 100871, China, and [¶]School of

Engineering, Brown University, Providence, Rhode Island 02912, USA

E-mail: xyi@pku.edu.cn; huajian_gao@brown.edu

CGMD simulations: Methodology and interaction potentials

In our CGMD simulations, the non-bonded bead-bead interactions are described by potentials U_{WCA} and U_{COS}, and the bonded bead-bead interactions are described by potentials U_{FENE} and U_{harmonic} as follows.

$$U_{\text{WCA}}(r) = 4\varepsilon \left[(\alpha\sigma_{\text{b}}/r)^{12} - (\alpha\sigma_{\text{b}}/r)^6 + 1/4 \right] \qquad (0 < r < r_{\text{cut}}),$$

$$U_{\text{COS}}(r) = \begin{cases} -\varepsilon + U_{\text{WCA}}(r) & (0 < r < r_{\text{cut}}), \\ -\varepsilon\cos^2\left[\pi(r - r_{\text{cut}})/(2w)\right] & (r_{\text{cut}} < r < r_{\text{cut}} + w), \end{cases}$$

$$U_{\text{FENE}}(r) = -\tfrac{1}{2}k_{\text{FENE}}r_\infty^2 \ln\left(1 - r^2/r_\infty^2\right) \qquad (0 < r < r_\infty),$$

$$U_{\text{harmonic}}(r) = \tfrac{1}{2}k_{\text{harmonic}}(r - r_0)^2,$$

where $r_{\text{cut}} = 2^{1/6}\alpha\sigma_{\text{b}}$, ε and σ_{b} are the energy well depth and bead diameter, respectively. Values of parameters α and w in the non-bonded interaction potentials are listed in Table S1. The bead diameter σ_{b} is set to be 1 nm to construct a lipid bilayer with an appropriate membrane thickness and area per lipid. To ensure the mechanical properties of the lipid membrane falling in a range measured experimentally, we chose ε as $0.56 \text{ kcal}\cdot\text{mol}^{-1}$, which scales the unit thermal energy as $k_{\text{B}}T = 1.1\varepsilon(T = 310 \text{ K})$. Each lipid molecule is approximated by three connected beads with one hydrophilic head bead and two hydrophobic tail beads. The nearest neighbor beads in each lipid molecule are connected by FENE bonds with $k_{\text{FENE}} = 30\varepsilon = 16.8 \text{ kcal}\cdot\text{mol}^{-1}\cdot\text{nm}^{-2}$ and $r_\infty = 1.5\sigma_{\text{b}} = 1.5$ nm. The head bead is also connected to the second tail bead by a harmonic bond with a rest length $r_0 = 4\sigma_{\text{b}} = 4$ nm and force constant $k_{\text{harmonic}} = 10\varepsilon = 5.6 \text{ kcal}\cdot\text{mol}^{-1}\cdot\text{nm}^{-2}$. Nanorods of different sizes were constructed by multi-walled coarse-grained beads folded from two-dimensional triangular lattices with nearest beads of distance 1.3σ. Different shapes of the nanorods were constructed by deleting the corresponding redundant beads from the cylindrical nanorods. Fig. S1a shows selected nanorods of different sizes and shapes. To illustrate how the encapsulated nanorod is created, we take the cylindrical nanorod as an example. A short nanorod consisting of two equal parts, each of length 20 nm, was first put at the center of a vesicle of radius 50 nm. Then these two parts were pulled slowly in opposite directions at a constant speed (1 m/s) in the simulations. Eventually the intermediate trajectory (Fig. S1b) was obtained and used to create

the initial model of the encapsulated nanorod by replacing these two separated parts with a single nanorod (Fig. S1c). Encapsulated nanotubes of non-uniform diameters are built following a similar scheme. With the initial system configurations shown in Fig. S1c for nanorods of different sizes, the CGMD simulations were performed under a constant ambient temperature with a time step fixed at 100 fs. The encapsulated nanorod was fixed while the vesicle membrane was allowed to move freely during simulations. After equilibrium is reached, a 100 ns simulation is performed and we split the nanorod into two parts (as demonstrated in Fig. S1d). As the nanorod is fixed, the axial contact force on each nanorod part equals to the balancing force, a total force on each part which is determined and recorded by LAMMPS. Fig. S1e shows the time evolution of the axial contact force and the corresponding averaged value in the case of a uniform nanorod at $a/R = 0.2$ and $L/R = 4.2$ from MD simulations.
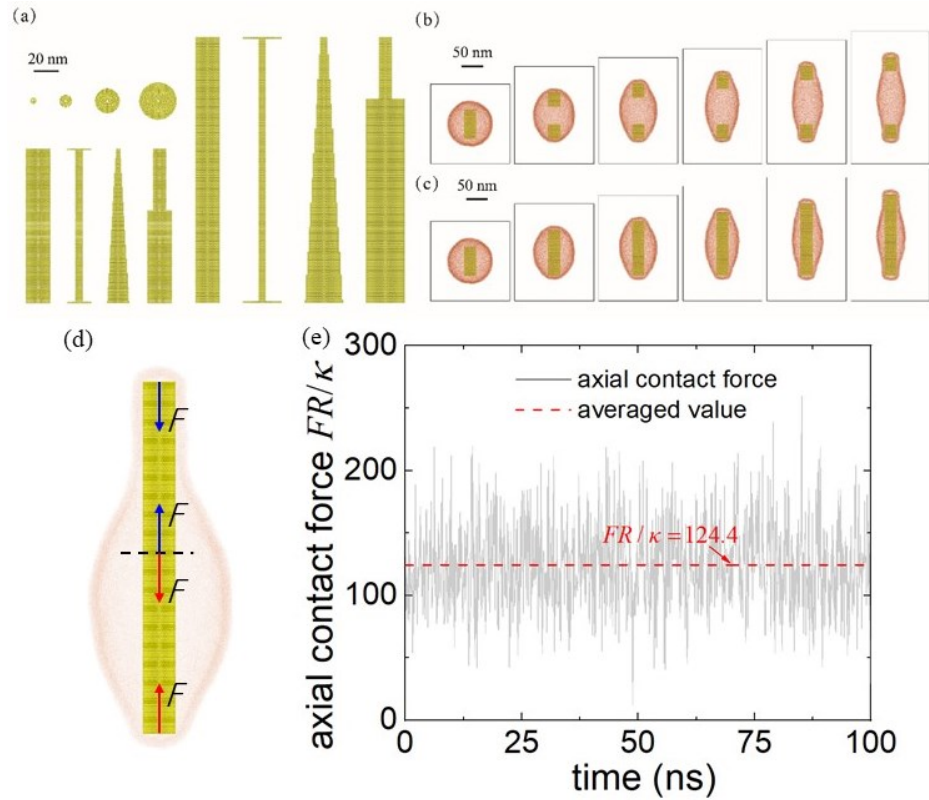

Fig. S1: (a) Selected examples of coarse-grained model of nanorods of different sizes and shapes. (b) Time sequences of a pulling simulation scheme. (c) The initial system configurations of vesicles encapsulating cylindrical nanorods of different lengths. (d) The equilibrium configuration used to determine the axial contact force. (e) Time evolution of the axial contact force and the corresponding averaged value in the case of a uniform nanorod at $a/R = 0.2$ and $L/R = 4.2$ from the MD simulations.

Results from theoretical analysis and MD simulations

Fig. S2 shows that the membrane tension σ gradually increases to a peak, followed by severe declines initiating with or exhibiting a discontinuous drop. Note that σ at a large L could be significantly smaller than that at $L/R = 2$.

Table S1: Parameters of non-bonded interactions.

bead type	bead type	interaction	parameters
lipid head	lipid head	WCA	$\alpha = 0.95$
lipid head	lipid tail	WCA	$\alpha = 0.95$
lipid tail	lipid tail	COS	$\alpha = 0.95, w = 1.6\sigma$
nanorod	lipid head/tail	WCA	$\alpha = 0.95$
nanorod	nanorod	WCA	$\alpha = 0.95$
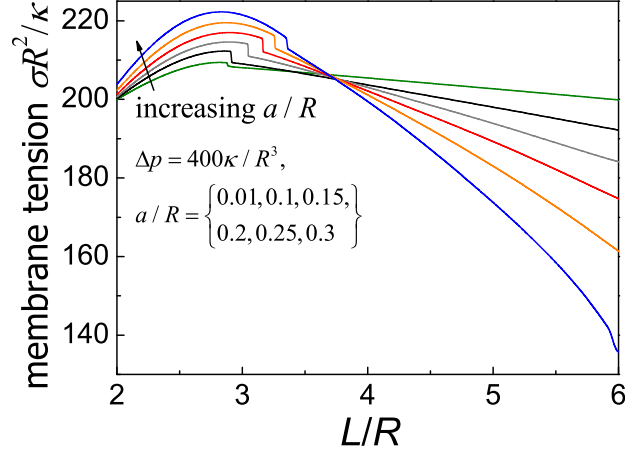
Fig. S2: Normalized membrane tension $\sigma R^2/\kappa$ as a function of the normalized nanorod length L/R for different values of the normalized nanorod radius a/R.
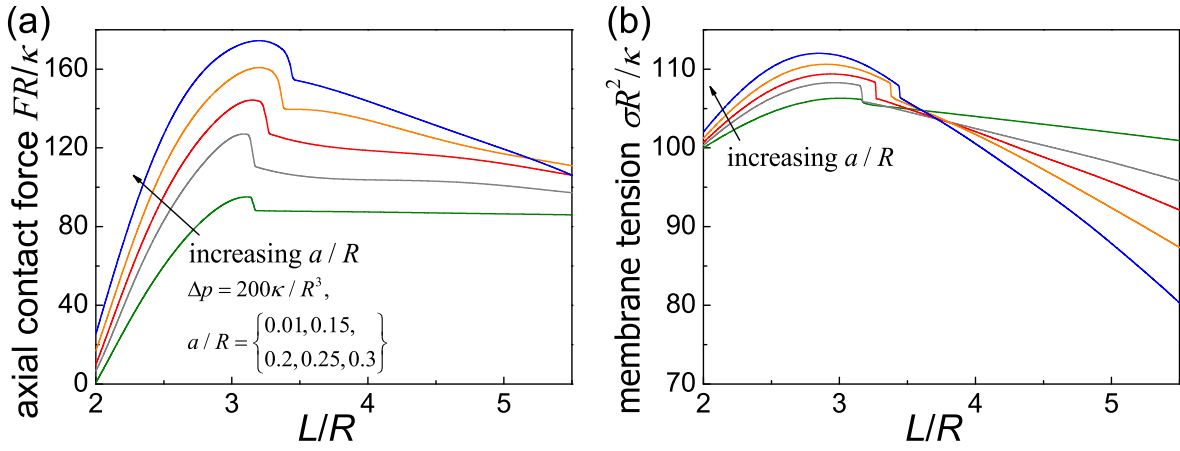

Fig. S3: (a) Normalized effective axial contact force FR/κ and (b) normalized effective membrane tension $\sigma R^2/\kappa$ as functions of L/R at $\Delta p = 200\kappa/R^3$.

For the vesicle at a fix pressure difference $\Delta p = \beta \kappa/R^3$, decreasing (or increasing) the vesicle size is equivalent to decrease (or increase) the parameter β. To investigate the effect of the vesicle size on the mechanical interplay between the encapsulated nanorod and the vesicle, we perform case studies of $\beta = 200$ (Fig. S3) as a comparison case with $\beta = 400$ in the main text. Though both

the normalized axial contact force FR/κ and membrane tension $\sigma R^2/\kappa$ decrease as β decreases, the trends are quite similar to the case of $\beta = 400$ (Figs. 2a and S2). As $\Delta p \sim \beta$ for a certain vesicle, we can also conclude that the axial contact force and membrane tension increase as the pressure difference increases.
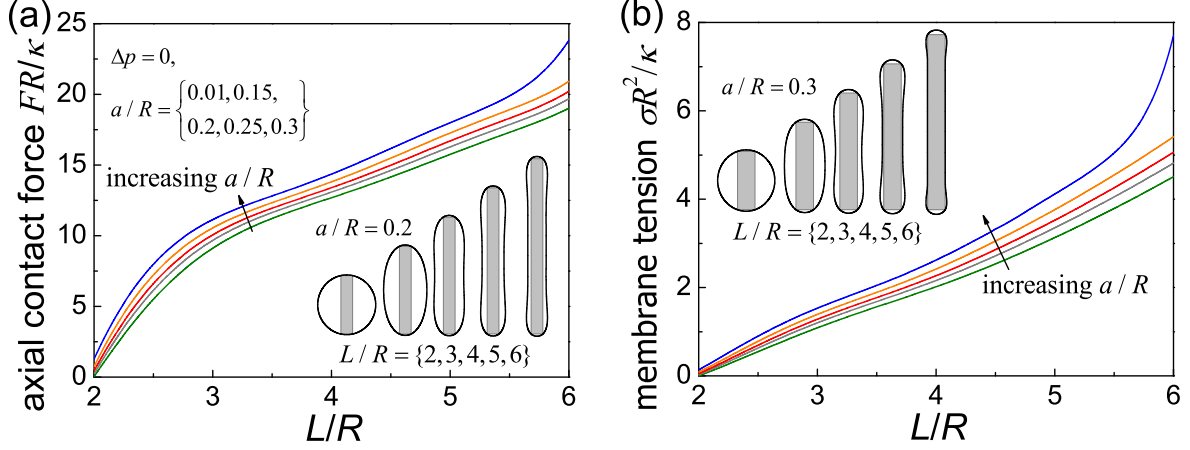

Fig. S4: (a) Normalized effective axial contact force FR/κ and (b) normalized effective membrane tension $\sigma R^2/\kappa$ as functions of L/R at zero pressure difference. The vesicle morphologies at $a/R = 0.2$ and 0.3 and selected lengths are shown in insets in (a) and (b), respectively.
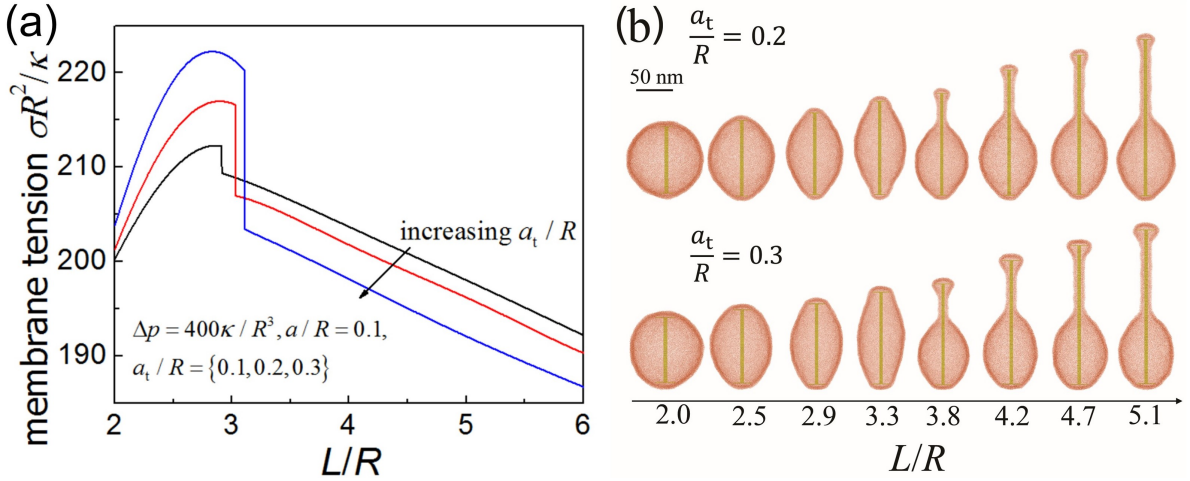

Fig. S5: (a) Normalized effective membrane tension $\sigma R^2/\kappa$ as a function of the normalized length L/R of a straight nanorod with two widened tips. Here a and a_t represent the radii of the rod wall and tip, respectively. (b) The vesicle morphologies from MD simulations for $\Delta p = 100\kappa/R^3$.

The mechanical response of the vesicle to the encapsulated nanorod at zero pressure difference is significantly different from that at $\Delta p = 200\kappa/R^3$ and $400\kappa/R^3$. Compared to the nonmonotonic feature of the force and tension curves at $\Delta p = 200\kappa/R^3$ and $400\kappa/R^3$ (Figs. 2a, S2, and S3), both curves of F and σ at $\Delta p = 0$ are smooth and monotonically increasing functions of L/R, as shown in Fig. S4. No membrane protrusion and discontinuous shape transformation of the vesicle are observed. As L increases, the vesicle maintains a tube-like shape but gradually becomes thinner.

4

An intriguing feature of the force curve in the case of $a/R = 0.3$ is that F increases at a much higher rate beyond a certain value of L/R around 5.5. This feature is due to the formation of contact between the rod wall and vesicle membrane.

In the case of an encapsulated straight nanorod with two widened tips, the membrane tension first increases and gradually rises to a maximum. Upon the vesicle tubulation and the initiation of contact between the vesicle membrane and rod wall, the membrane tension decreases linearly with respect to L/R (Fig. S5a). More vesicle morphologies from MD simulations in addition to these in the inset in Fig. 5b could be found in Fig. S5b.
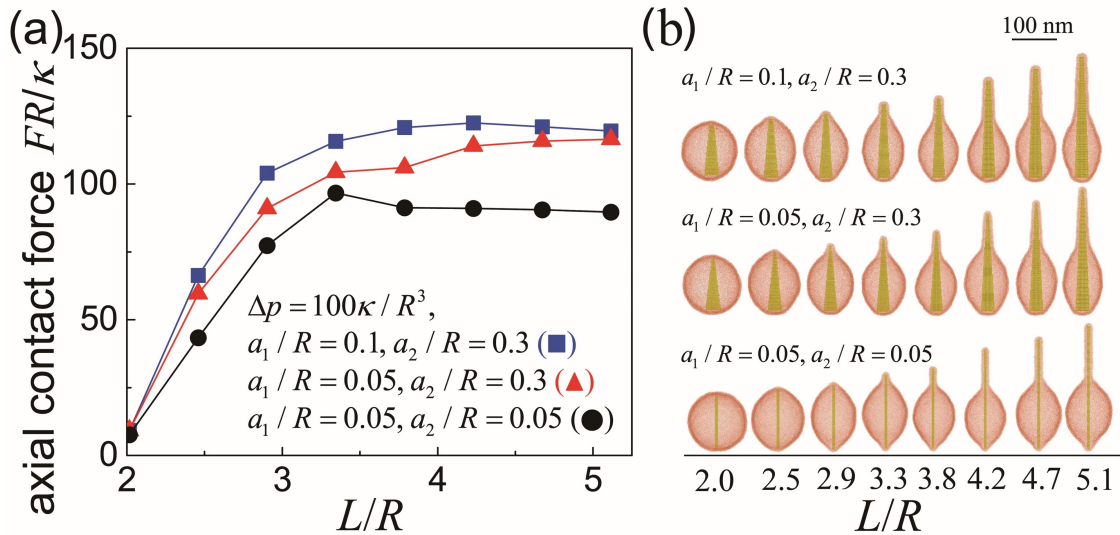

Fig. S6: (a) Normalized axial contact force FR/κ as a function of the normalized nanorod length L/R. (b) Vesicle morphologies induced by cone-shaped nanorods from MD simulations.
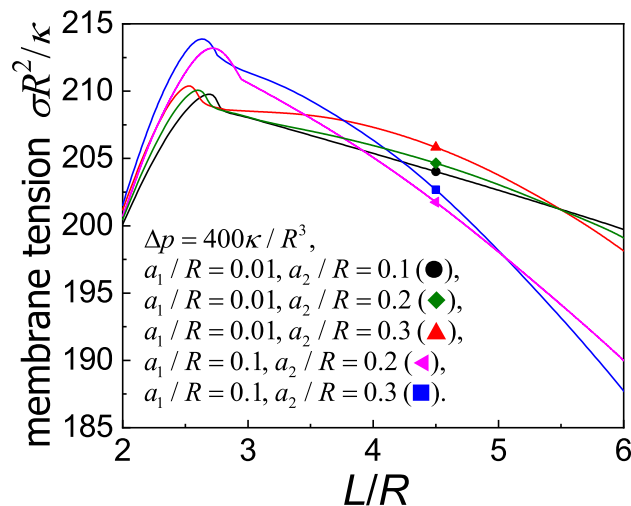

Fig. S7: Normalized effective membrane tension $\sigma R^2/\kappa$ as a function of the normalized length L/R of encapsulated cone-shaped nanorods at $\Delta p = 400\kappa/R^3$. Here a_1 and a_2 represent radii of the top and bottom ends of the nanorods.

The axial contact force curves and vesicle morphologies for encapsulated cone-shaped nanorods from MD simulations are shown in Fig. S6. No lemon-shaped vesicles with mirror symmetry are observed in MD simulations, and the tubular membrane protrusions always occur from the vesicle pole in contact with the smaller nanorod end. We did not observe the force peak associated with vesicle tubulation in MD simulations as it is located in a narrow range of L/R as predicted theoretically in Fig. 6. As the length of the nanorod or the tubular membrane protrusion increases, the radius of the protrusion increases. Consequently, the axial contact force increases as L/R increases. MD simulations and theoretical analysis predict similar vesicle morphologies.

In the case of cone-shaped nanorods, the membrane tension gradually increases to a peak, and then decreases smoothly as L/R further increases (Fig. S7). Compared to a straight nanorod of uniform radius, the tension peaks in the case of cone-shaped nanorods occur at smaller L/R, and the rates of post-peak decreasing are lower.

In the case of a screwdriver-shaped nanorod, both F and σ exhibit two local maxima (Fig. S8). The first local maximum is due to the formation of a tubular membrane protrusion enclosing the upper portion of the nanorod, and the second local maximum is due to the growing protrusion enclosing the lower portion of the nanorod. MD simulations in Fig. S9a show similar trends of the axial contact force as our theoretical results in Fig. S8a. In the case of $a_2/R = 0.3$, two force peaks are observed and the first force peak arises from the initial vesicle tubulation enclosing the upper portion of the nanorod (Fig. S9b). As the membrane protrusion comes to contact with the lower portion of the nanorod, the second force peak emerges, and after that the axial contact force decreases with L, as predicted by our theoretical analysis. Selected morphologies of the vesicles encapsulating the screwdriver-shaped nanorods are shown in Fig. S9b.
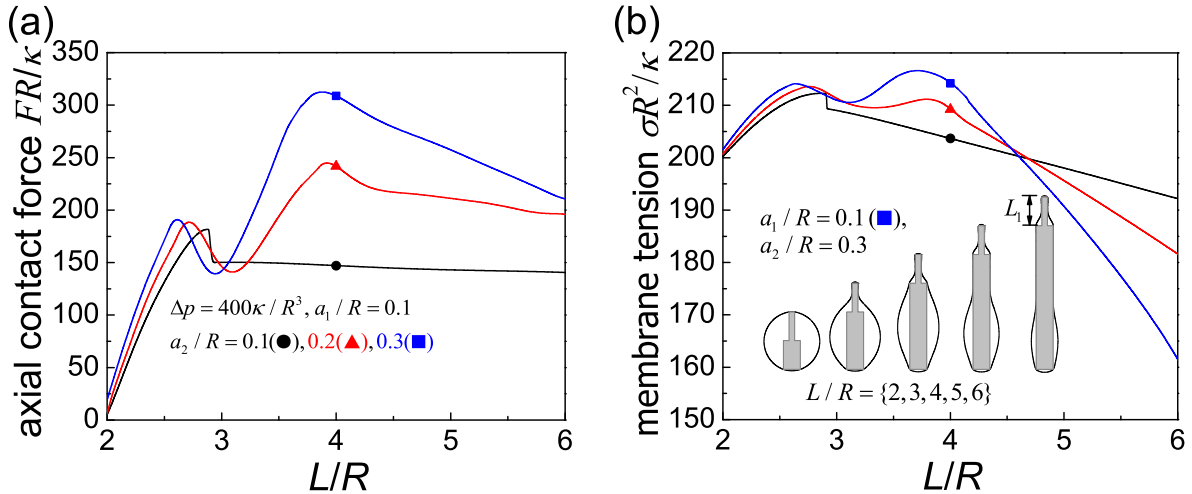

Fig. S8: Normalized effective axial contact force FR/κ (a) and normalized effective membrane tension $\sigma R^2/\kappa$ (b) as functions of the normalized length L/R of screwdriver-shaped nanorods. Inset in (b) plots the vesicle morphologies induced by encapsulated screwdriver-shaped nanorods of different radial sizes $a_2/R = 0.1, 0.2$, and 0.3 and lengths $L/R = 2, 3, 4, 5$, and 6. Here a_1 and a_2 represent radii of the top and bottom parts of the screwdriver-shaped nanorods, and we take $a_1/R = 0.1$ and $L_1/R = 1$. Inset in (b) plots the vesicle configurations at $a_1/R = 0.1$ and different values of L/R.
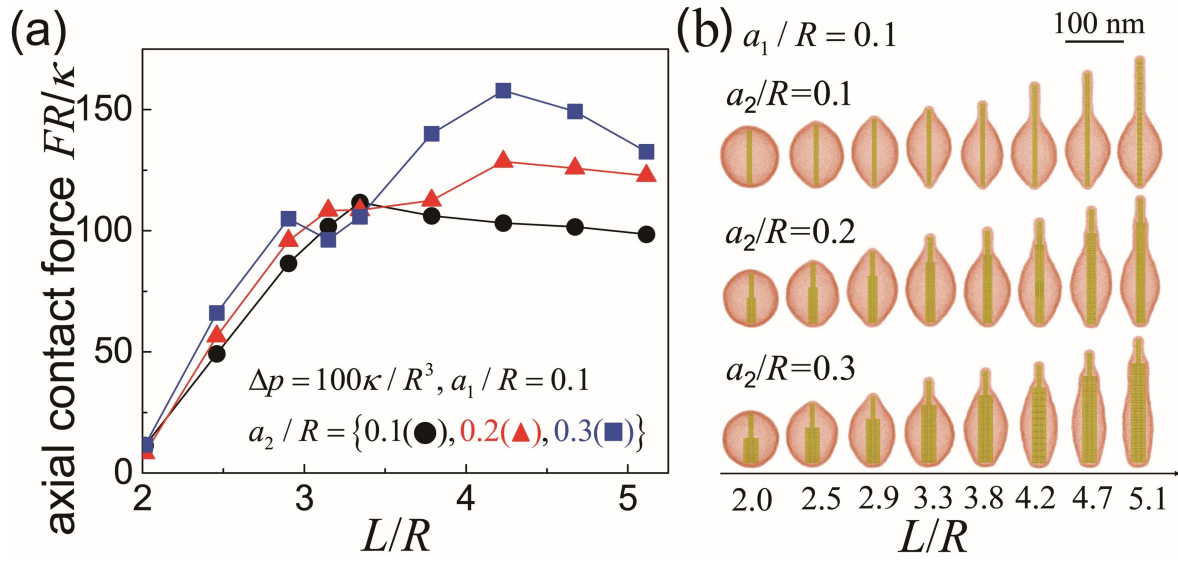
Fig. S9: (a) Normalized axial contact force FR/κ as a function of the normalized length L/R of screwdriver-shaped nanorods at $\Delta p = 100\kappa/R^3$ and $a_1/R = 0.1$, and (b) selected vesicle morphologies from MD simulations.